Sustainable Energy & Fuels

ROYAL SOCIETY OF CHEMISTRY

PAPER

View Article Online
View Journal | View Issue

Cite this: *Sustainable Energy Fuels*, 2026, **10**, 1705

MgO/CuO modified stainless steel mesh cathode for enhanced CO_2 reduction to biomethane in a microbial electrosynthesis system

Simran Kaur Dhillon, Tae Hyun Chung and Bipro Ranjan Dhar *

The microbial electrosynthesis system (MES) offers an attractive platform for effective cathodic reduction of carbon dioxide (CO_2) to biomethane (CH_4). However, achieving high productivity and energy efficiency remains challenging, often due to sluggish hydrogen evolution reaction (HER) kinetics at the cathode. Here, we showed an efficient CO_2 reduction reaction with a stainless steel mesh cathode electrodeposited with magnesium oxide (MgO) and copper oxide (CuO); MgO/CuO-SSM. The electrodes are coupled with an enriched anaerobic culture to facilitate the bioproduction of CH_4 from CO_2. Material characterization confirmed the successful deposition of MgO and CuO on SSM, while electrochemical analysis revealed superior catalytic performance of the composite electrode compared to bare SSM. Furthermore, optimizing the applied cathode potential from −1 V to −0.9 V *vs.* Ag/AgCl/KCl (sat'd) for modified SSM improved the methane production while increasing the electrical energy efficiency. At −0.9 V *vs.* Ag/AgCl/KCl (sat'd), MgO/CuO-SSM recorded an energy efficiency of 21.6% (103.8 ± 3.8 L(CH_4) m^{-3}(catholyte replaced) d^{-1}), surpassing that of bare SSM (14.7%, 117.5 ± 3.6 L(CH_4) m^{-3}(catholyte replaced) d^{-1}) operated at −1 V *vs.* Ag/AgCl/KCl (sat'd). Overall, our work introduces a promising and facile electrode modification strategy that enhances MES performance, enabling CO_2 reduction to CH_4 at reduced energy demand towards practical carbon neutrality applications.

Received 6th November 2025
Accepted 11th February 2026

DOI: 10.1039/d5se01460c

rsc.li/sustainable-energy

1. Introduction

Microbial electrolysis has emerged as an attractive bioelectrochemical process, enabling the conversion of CO_2 and biogas into biomethane and other valuable products traditionally derived from fossil fuels. Within the MES, the reduction of carbon dioxide (CO_2) into methane (CH_4) is particularly attractive, as methane can serve as a renewable biofuel with an energy density of 55.5 MJ kg^{-1}.[1] The first proof-of-concept study demonstrated CO_2 reduction at the cathode of the MES, where chemolithoautotrophic microbes fixed CO_2 *via* direct or mediated electron transfer.[2] Several studies have described multiple pathways through which CO_2 is converted to CH_4 in the MES,[3,4] with increasing interest in methanogenic biocathodes. In an MES, mixed-culture microorganisms enriched with methanogens can catalyze the CO_2 reduction to biomethane *via* multiple pathways: (a) *direct electromethanogenesis*, where electroactive methanogens directly reduce CO_2 to CH_4; (b) *hydrogen-mediated methanogenesis*, where hydrogen (H_2) produced at the cathode *via* the hydrogen evolution reaction (HER) is subsequently consumed by hydrogenotrophic methanogens to form CH_4;[5] and (c) *acetogenesis*, where bacteria convert CO_2 into acetate, which can later be metabolized to CH_4 by acetoclastic methanogens.[6]

(a) Direct electromethanogenesis

$$CO_2 + 8H^+ + 8e^- \rightarrow CH_4 + 2H_2O \quad \text{(i)}$$

(b) H_2-mediated pathway

$$2H^+ + 2e^- \rightarrow H_2 \text{ or } 2H_2O + 2e^- \rightarrow H_2 + 2OH^- \quad \text{(ii)}$$

$$CO_2 + 4H_2 \rightarrow CH_4 + 2H_2O \quad \text{(iii)}$$

(c) Acetate-mediated pathway

$$CO_2 + 8H^+ + 8e^- \rightarrow CH_3COO^- + 2H_2O \quad \text{(iv)}$$

$$CH_3COO^- + H^+ \rightarrow CH_4 + CO_2 \quad \text{(v)}$$

In a typical MES operation, current is generated at the anode electrode *via* water splitting, while the hydrogen evolution reaction (HER) occurs at the cathode. Although cathodic microbes are inherently capable of reducing CO_2, the natural reaction rate is too slow for practical applications. Thus, applying an external cathode potential accelerates electron transfer, thereby enhancing CO_2 reduction.[7] A negative potential applied to the cathode drives the electrochemical synthesis reaction, generating protons *via* water electrolysis at the anode.

Department of Civil and Environmental Engineering, University of Alberta, 9211-116 Street NW, Edmonton, AB, Canada, T6G 1H9. E-mail: bipro@ualberta.ca

Since the cathode, as an electron donor, is crucial for regulating reaction kinetics, product yields, and CH_4 production rate, it is necessary to control the cathode potential, which governs the HER and provides the driving force for CO_2 reduction to biomethane.[8] Thus, an efficient H_2 production and consumption rate is crucial for enhancing biomethane production. The thermodynamic threshold cathode potential for the HER is approximately −0.6 V *vs.* Ag/AgCl at neutral pH. However, electrode overpotentials typically shift the operational cathode potential to more negative values. Based on pathways facilitated by reactions (i) and (ii), at cathode potentials more negative than −0.613 V *vs.* Ag/AgCl, abiotic H_2 evolves along with a combination of direct electron transfer from the cathode to methanogens and indirect H_2-mediated electron transfer based on the microbial community response. At a less negative cathode potential (<−0.443 V *vs.* Ag/AgCl), abiotic H_2 evolution needs to be minimized due to thermodynamic limitations of the HER. This leads to CO_2 reduction according to reaction (i).[62] Electroactive biofilms on cathodes can improve the coulombic and energy efficiencies.[9] Nonetheless, low solubility and mass transfer limitations may reduce H_2 utilization efficiency and adversely affect CO_2 conversion.[10] Furthermore, a strong C–H bond, sluggish multi-electron transfer process, and proton-coupling requirements impose limitations on selectivity.[11]

Given these challenges, the energy efficiency of the MES is another crucial aspect that requires immediate attention, as it governs the practical transition of the lab-scale MES concept into a commercially competitive renewable technology. It provides insight into the sustainability, scalability, and economic viability of the process for producing value-added products such as methane. An MES with low impedance is therefore necessary to improve the overall efficiencies. Recently, a zero-gap MES cell operated at an applied cell voltage of 3.1 V exhibited a low ohmic resistance of 2.4 mΩ m^2 and methane production of 3 ± 1 L L^{-1} d^{-1}.[12] Another study reported a methane production rate of 7 L L^{-1} d^{-1} with an energy efficiency of 27% at a set current of 35 A m^{-2}.[13] A higher methane production rate of 16 L L^{-1} d^{-1} was achieved using granular activated carbon-based cathodes, though at a high applied cell voltage of 3.7 V, the energy efficiency was compromised.[14] In another study, an MES equipped with dual-layered cathodes exhibited the same methane production (16 L L^{-1} d^{-1}) at a lower applied cell voltage of 2.8 V and improved energy efficiency of 34%. While dual-layer cathodes improved methane production, high hydrogen accumulation in biogas remained a challenge at high current densities.[15] Thus, cathode materials with high conductivity, biocompatibility, large surface area, and corrosion resistance are critical, as they directly influence microbial colonization, electron transfer efficiency, and ultimately MES performance.[16–18] Stainless steel is often employed as a cathode electrode in the MES due to its relatively low HER overpotential and cost-effectiveness, although its performance is limited.[19–21] Among non-precious-metal catalysts, copper (Cu) and Cu-derived catalysts have been extensively investigated for abiotic CO_2 reduction, achieving high activity while producing other organics such as acetate, formate, ethanol, and methanol, which could serve as good substrates for some methanogens.[22–24]

For the MES, biofilm formation on the cathode surface and CO_2 reduction at the applied cathode potential should be considered to adopt Cu biocathodes. While Cu exhibits good conductivity and catalytic activity, it may not provide suitable surface properties for microbial adhesion in the MES.[25,26] To overcome the biofilm limitation, strategies such as metal deposition on biocompatible carbon-based materials and dual-layer metal composite electrodes have been explored.[15,27] Beyond transition metals and their oxides, alkali earth metals such as magnesium (Mg) have emerged as promising alternatives for advancing electrocatalytic activity.[28] In particular, magnesium oxide (MgO) is considered an environmentally friendly and versatile material with a low coordination number and abundant surface vacancies, features that enable its application in catalysis, superconductors, and batteries.[29] When applied as a coating on cathode surfaces, MgO has been shown to extend electrode life and improve the performance of various electrochemical systems, such as batteries, fuel cells, and electrolyzers.[30] A recent computational study further suggested that Mg can facilitate CO_2 conversion to CH_4, accompanied by the HER. Its effect was attributed to the high surface area of Mg nanoparticles, which enhances CO_2 adsorption, surface activation and subsequent reduction of surface-bound CO_2.[31] However, experimental validation of these findings remains scarce.

In this study, we designed a 3D blossom-like composite electrode comprising MgO and CuO nanostructures *via* electrodeposition on stainless steel mesh (SSM), representing a promising modified cathode catalyst for the MES. Self-supported CuO-modified SSM was first fabricated and subsequently used as a substrate for the deposition of hierarchical bloom-like MgO structures, forming a MgO/CuO-SSM composite. The presence of dual metal sites is expected to synergistically enhance absorption capacity, electrical conductivity, and overall electrochemical activity. To evaluate the performance, dual-chambered MESs were operated initially at an applied cathode potential of -1 V *vs.* Ag/AgCl/KCl (sat'd), followed by operation at −0.9 V *vs.* Ag/AgCl/KCl (sat'd) for modified electrodes (SSM was maintained at −1 V *vs.* Ag/AgCl/KCl (sat'd)). CuO deposition on SSM and lower cathode potentials are likely to enhance the HER, influencing the H_2-mediated pathway (b) for CH_4 production. While MgO improves the wettability of the electrodes, which is essential for biofilm formation and H_2 utilization, it indirectly supports the H_2-mediated pathway (b) and the acetate-mediated pathway (c). To the best of our knowledge, this is the first study to demonstrate the application of combined MgO and CuO nanostructures on SSM cathodes for enhanced electrochemical reduction of CO_2 to CH_4 in the MES.

2. Materials and methods

2.1 Materials

High-purity magnesium nitrate hexahydrate ($Mg(NO_3)_2 \cdot 6H_2O$), copper sulphate hexahydrate ($CuSO_4 \cdot 5H_2O$), and sodium

sulfate (Na_2SO_4) are from Sigma–Aldrich Chemical Ltd. and used without further treatment. The current collector was stainless steel mesh (SS, grade T304, 70 mesh) purchased from McMaster-Carr, USA. SSM has a pore size of 0.02 cm and a wire diameter of 0.016 cm, while the platinized titanium (Pt/Ti) fibre felt (592796-2, platinized titanium fibre felt) was received from Fuel Cell Store, Texas, USA. Proton exchange membrane (PEM) Nafion™ 117 was obtained from TheSix Technology Solutions, Toronto, Canada. For connections, a titanium wire (TA2, GOONSDS, China) of a 0.2 mm diameter was used. H-cell type reactors with a working volume of 250 mL in each chamber were used as the MES. They were purchased from LaborXing, Shenzhen, China. Ag/AgCl/KCl (sat'd) (MF-2052) was received from Bioanalytical System Inc., West Lafayette, IN, USA. The potentiostat (Squidstat Prime, serial number: 1066) was acquired from Admiral Instruments, Arizona, USA.

2.2 Fabrication of modified electrodes

SSM (T304 grade) electrodes were cut into rectangular pieces (4 × 3 cm^2) and sonicated in 1 M hydrochloric acid (HCl), deionized (DI) water, and acetone for 10 min each to remove any contaminants and surface oxides. Finally, the electrodes were washed and stored in deionized water prior to use. CuO nanoparticles were electrodeposited on pretreated SSM through a series of electrochemical deposition and heat treatment processes. The synthesis was performed according to a reported method with slight modifications.[32] Typically, a SSM electrode (4 × 3 cm^2) was soaked in 200 mL of deionized water to which 1.493 g of $CuSO_4 \cdot 5H_2O$ was added and stirred well for 2 h. To this, 2.84 g $NaSO_4$ was introduced under continuous stirring to ensure uniform composition. An external cathode potential of −1 V *vs.* SCE was applied for 1500 s to initiate the electrodeposition of Cu intermediates. The electrodeposited electrode was rinsed with deionized water and calcined at 400 °C for 2 h in a muffle furnace to obtain CuO-SSM for use.

3D hierarchical MgO nanostructures were subsequently deposited onto the CuO-SSM electrode *via* galvanostatic electrodeposition. The CuO-SSM electrode was immersed in an aqueous solution of 0.2 M $Mg(NO_3)_2 \cdot 6H_2O$ (5.128 g in 100 mL deionized water) for 1 h prior to deposition. A constant current density of 20 mA cm^{-2} was applied for 20 min under continuous stirring.[33] The as-prepared electrode was rinsed and subjected to heat treatment using a programmable temperature ramp: room temperature to 450 °C at a rate of 2 °C min^{-1}, followed by isothermal hold at 450 °C for 60 min (Fig. 1), ensuring complete decomposition of magnesium nitrate and MgO formation. To examine the material properties, MgO-SSM was synthesized using a method similar to that for bare SSM.

2.3 MES configuration and operation

Dual-chamber MES reactors were operated in semi-batch cycle mode at room temperature. Each reactor had a total working volume of 500 mL, divided equally between the cathode and anode chambers (250 mL). Each reactor chamber featured three sidearms, with an anode and cathode chamber separated by a Nafion™ 117 proton exchange membrane (exposed geometric area, 9.08 cm^2). Prior to use, the membranes were sequentially pretreated in 3% H_2O_2, deionized water, and 3% H_2SO_4 at 70–80 °C for 1 h each, followed by thorough rinsing and storage with deionized water until use.[34] MES reactors were equipped with a Pt/Ti anode (exposed geometric area, 24 cm^2), modified SSM-based cathode (SSM, CuO-SSM, or MgO/CuO-SSM; exposed area, 24 cm^2), and Ag/AgCl/KCl (sat'd) reference electrode positioned in the cathode chamber through the sidearm, maintaining an appropriate distance from the electrode (Fig. S1). The membrane was sandwiched between rubber gaskets. All joints were sealed to maintain a fixed seal, ensuring that each reactor remained gas-tight and leak-proof. The cathode chamber was filled with a growth medium containing bicarbonate as the inorganic carbon source (pH = 7–7.3), composed of 3.33 g L^{-1} Na_2HPO_4, 12 g L^{-1} NaH_2PO_4, 0.5 g L^{-1} NH_4Cl, 4 g L^{-1} $NaHCO_3$, and 1 mL L^{-1} trace mineral solution.[35] Prior to the operation, the catholyte medium was purged with high-purity nitrogen gas for 30 min to achieve anaerobic conditions. The anode chamber was filled with regular tap water.

The cathode (working electrode) and the anode (counter electrode) were connected to a potentiostat operated at a fixed cathode potential. The initial applied cathode potential (−1 V *vs.* Ag/AgCl/KCl (sat'd)) was selected based on our previous studies.[35] All sidearms and screw caps were sealed with silicon septa, and 500 mL gas sampling bags were fitted to the reactor headspace to collect the gas produced. The reactors were operated at room temperature under constant stirring.

For cathode biofilm enrichment, the inoculum consisted of effluents from an existing MES reactor[35] and MEC-AD reactor (100 mL total), supplemented with 10 mL of anaerobic digestate sludge collected from the local wastewater treatment plant in Edmonton, Canada. During preliminary studies, reactors were operated at −1 V *vs.* Ag/AgCl/KCl (sat'd) for 2 months to allow stable microbial biofilm formation. During this period, the catholyte was partially replenished every 4 days, while the anolyte was replenished to compensate for water loss. Catholyte pH was maintained at 7.2 ± 0.3 using 0.2 M HCl, and the anolyte pH was adjusted to <3. Following enrichment, all reactors were operated in semi-batch mode to assess MES performance. The catholyte was replaced with fresh medium and purged with nitrogen prior to each cycle. For reactors equipped with modified electrodes, the applied cathode potential was subsequently reduced to −0.9 V *vs.* Ag/AgCl/KCl (sat'd) to investigate catalytic performance at a lower energy input while maintaining sufficient driving force for the HER and methanogenesis. The reported data represent average current density (normalized to the geometric cathode area) and gas productivity (normalized to catholyte volume replaced per cycle), calculated from two consecutive 4-day semi-batch cycles. Energy yields of different MES reactors were determined.[63] The net energy yield (W_{net}) was calculated in J according to eqn (vi), where W_e (in J) represents the total electrical energy consumed across different cathode systems, and W_{CH_4} (in J) is the total energy output corresponding to the methane gas produced.

$$W_{net} = W_{CH_4} - W_e \quad \text{(vi)}$$

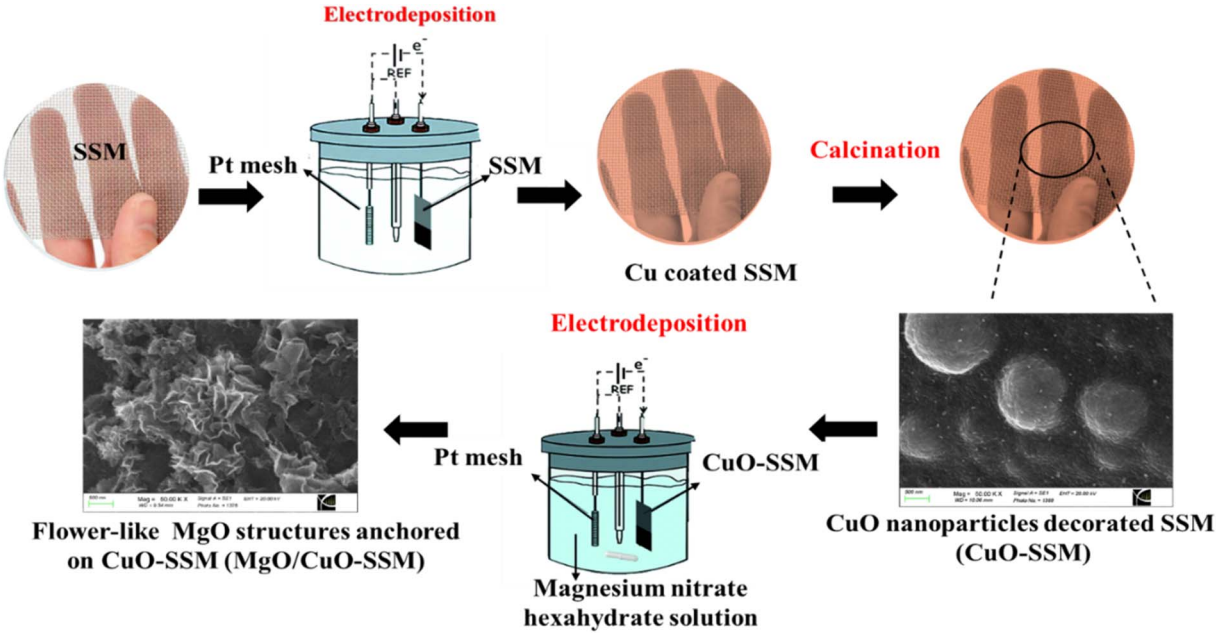

Fig. 1 Step-by-step MgO/CuO-SSM cathode fabrication protocol.

The energy content of the methane, W_{CH_4}, was a product of the heat of combustion of methane ($\Delta H_s = 890\,310$ J mol^{-1}) and total moles of methane generated in a cycle. W_e is computed by the product of the applied voltage and the cumulative coulombs. Energy efficiency per cycle is expressed as the ratio of the energy content of CH_4 (based on its heat of combustion) produced to the electrical energy input (from the applied cathode potential).

2.4 Material characterization and analysis

X-ray diffraction (XRD) analysis was conducted using a Rigaku Ultima IV diffractometer from Rigaku Corporation equipped with a cobalt tube radiation source at 38 kV and 38 mA. The data obtained were converted using JADE MDI 9.6 software and phase identification was done using DIFFRAC.EVA V5 software. The patterns were matched with the 2023/2024 ICDD PDF 5+ and the crystallographic open database. The hydrophilicity/hydrophobicity of the synthesized catalysts was analyzed using a drop shape analyzer (Kruss DSA100E) equipped with a motorized liquid syringe. Morphological characteristics were analyzed by ZEISS EVO 10 Scanning Electron Microscopy (SEM).

The electrocatalytic properties of the electrodes were characterized using cyclic voltammetry (CV), linear sweep voltammetry (LSV), and electrochemical impedance spectroscopy (EIS) in dual-chamber MES, separated by Nafion™ 117. The modified cathodes functioned as the working electrode, the Pt/Ti anode functioned as the counter electrode, and the Ag/AgCl/KCl (sat'd) reference electrode was positioned within 1 cm of the cathode. All potentials are reported *versus* the reference electrode. The electrochemical measurements were conducted at room temperature using a 5-channel modular potentiostat (VSP Multichannel Workstation, Biologic Science Instruments, USA), and data were processed using EC-Lab V-10.44 software. For CV analysis, cathode potential was scanned from +1 V to −1 V (*vs.* Ag/AgCl/KCl (sat'd)) at a scan rate of 5 mV s^{-1}. EIS measurements were conducted at an open-circuit voltage (OCV) across a frequency range of 100 kHz to 0.1 Hz with a 10 mV perturbation amplitude. The obtained EIS spectra were fitted to appropriate equivalent circuits to determine the charge transfer resistance and other key parameters. The total biogas produced was collected in leak-proof gas sampling bags connected to the cathode chamber of the MES reactor headspace. The composition of the collected gas was determined using a gas chromatograph (7890B, Agilent Technologies, Santa Clara, USA) equipped with a thermal conductivity detector (TCD). The H_2 production rate was quantified from the measured H_2 concentration in the total gas volume and normalized to the catholyte volume replaced and the time for each cycle. Thus, gas productivity per day is expressed as L (H_2) m^{-3}(catholyte replaced) d^{-1}, where L is the gas volume produced and m^3 is the volume of catholyte replaced after every cycle. The acetic acid in the catholyte samples was determined by high-performance liquid chromatography (HPLC), after filtering the samples through a 0.22 μm syringe filter. To determine the statistical significance of the findings, an unpaired *t*-test was conducted.

2.5 Microbial community analysis

The microbial communities present in the biofilms were extracted from the MEC and MFC anodes and identified using 16S rRNA-transcript sequencing. Biofilm samples were analyzed *via* Illumina Miseq sequencing, targeting the V4–V5 hypervariable region with primers 515F: 5′ GTGCCAGCMGCCGCGGTAA 3′ and 806R: 5′ GGACTACHVGGGTWTCTAAT 3'. Genomic DNA extraction was performed using DNeasy PowerSoil Pro Kits (QIAGEN, Hilden, Germany) following the manufacturer's protocol, and purity

and yield were assessed using a NanoDrop spectrophotometer (2000C, Thermo Scientific, USA). Extracted DNA samples were stored at −70 °C until sequencing at RTL Genomics, Lubbock, USA. The raw sequencing data were processed using the QIIME 2 pipeline, version 2022; https://qiime2.org.[36] Operational Taxonomic Units (OTUs) were assigned using UCLUST at 97% alignment against the Greengenes reference database (v. 13.8).[37] Alpha diversity matrices were computed *via* QIIME2 to assess microbial diversity under different conditions.

3. Results and discussion

3.1 Characterization of cathode electrodes

Fig. 2a and S2a present the XRD patterns of bare SSM and MgO/CuO-SSM. The crystallographic planes of CuO and MgO matched JCPDS (Joint Committee on Powder Diffraction Standards) standards 00-001-1117 and 01-075-1525, respectively. All diffraction patterns exhibit strong and sharp peaks corresponding to SSM. Since CuO is deposited as a thin surface layer, the characteristic reflections are relatively weak and appear with low intensity. For the MgO/CuO-SSM composite electrode, characteristic peaks for MgO and CuO were evident, with the main CuO peaks at 35.74° and 38.95° shifting slightly to 35.78° and 38.98° after MgO deposition (Fig. 2b). Although subtle, this shift towards higher diffraction angles suggests structural modification, possibly due to chemical interaction or Mg–Cu interface stress altering the CuO crystal structure.[38] Peaks corresponding to SSM matched JCPDS 04-022-7117 for $Cr_{0.5}Fe_{2.5}Al_{0.5}Si_{0.5}$ and COD 9016291 for Iron (Fe), with prominent peaks at 43.72°, 44.77°, and 50.93° corresponding to (111), (220), and (200) planes, respectively.[39] Other weak peaks were seen at 55.61° (222), 65.18° (400), and 71.88° (331). CuO-SSM exhibited multiple peaks at 35.74° (−111), 38.95° (111), 49.21° (−202), 53.88° (020), 58.76° (202), 66.22° (022), and 68.42° (220), characteristic of monoclinic CuO (tenorite),[40] with no evidence of other Cu oxides, confirming the formation of a single-phase material. Similarly, MgO-SSM showed peaks at 37.06°, 43.05°, and 62.53°, corresponding to the (111), (200), and (220) planes of periclase MgO.[33] Fig. 2c shows the water contact angle measurements of MgO-SSM and CuO-SSM electrodes. The contact angle followed the order: MgO/CuO-SSM (super hydrophilic, unmeasurable due to complete spreading) < MgO-SSM (14.6° ± 0.2°) < CuO-SSM (116.2° ± 0.1°). CuO-SSM exhibited a surface between hydrophobic (>90°) and superhydrophobic (≤145°). Dense agglomeration of CuO structures occurred on trapped air/gas pockets, imparting hydrophobicity to CuO-SSM,[41,42] which negatively affects the MES performance. In contrast, MgO is known to hydrate to $Mg(OH)_2$ in the aqueous phase, with the hydroxyl group (OH) imparting strong hydrophilicity.[43,44] Electrode wettability plays a pivotal role in CO_2 reduction as water affinity influences reactivity, stability, and selectivity.[45] Thus, MgO/CuO-SSM offers an optimal level of hydrophilicity that enhances ion diffusion. The interconnected MgO nanostructures are anticipated to reduce mass transfer limitations, thereby improving MES performance.

The morphology and microstructure of bare SSM and modified electrodes (MgO-SSM, CuO-SSM, and MgO/CuO-SSM) were examined by SEM. As shown in Fig. S2b and c, the bare

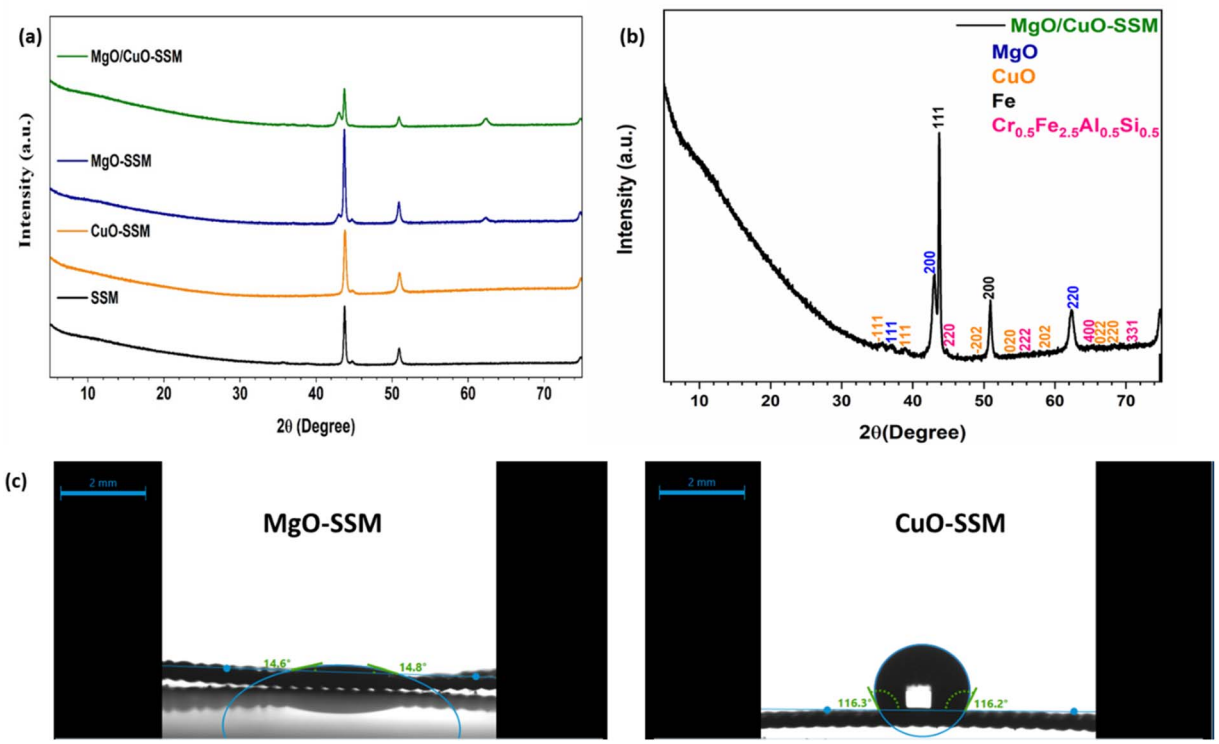

Fig. 2 XRD spectra of the electrodes (a); composite MgO/CuO-SSM catalyst (b); and water contact angle of water droplets on MgO-SSM and CuO-SSM surfaces (c).

SSM exhibited a smooth surface, whereas MgO-SSM (Fig. S2d and e) displayed a uniform coral-like coating, which enhanced the surface roughness and is expected to improve biofilm attachment and electrochemical activity.[46] The CuO-SSM electrode (Fig. 3a–c) exhibited a homogeneous layer of CuO nanoparticles uniformly distributed across its surface. These nanoparticles likely enhanced the electrode conductivity and electron transfer capacity compared to bare SSM.[32]

Upon electrodeposition of MgO on CuO-SSM, well cross-bonded $Mg(OH)_2$ structures were formed, which, after annealing at 450 °C for 1 h, transformed into distinctive flower-like MgO morphology anchored on the CuO-SSM surface (Fig. 3d–f). High magnification SEM images revealed that MgO nanostructures consisted of well-defined nano-petals with a lace-like texture, forming an interconnected framework. These 2D petal-like structures are expected to facilitate electrolyte ion diffusion and provide abundant active sites, thereby improving the electrochemical performance of the composite electrode.[33]

SSM is a cost-effective, conductive and corrosion-resistant material with low HER overpotential, making it a suitable alternative electrode for the HER.[35] However, its inert and smooth surface limits the active site density necessary for catalytic reactions. Incorporating metal oxides can enhance surface roughness and porosity, thereby improving catalytic performance. The LSV analysis revealed that, at an average operational current of −0.11 mA for all electrodes (Fig. 4a), bare SSM exhibits a potential for the HER of −0.63 V *vs.* Ag/AgCl/KCl (sat'd). Upon MgO deposition, the electrode potential shifted to −0.81 V *vs.* Ag/AgCl/KCl (sat'd), indicating that MgO does not act as an efficient HER catalyst and suppresses the activity of SSM. In contrast, CuO-SSM (−0.53 V *vs.* Ag/AgCl/KCl (sat'd)) and MgO/CuO-SSM (−0.44 V *vs.* Ag/AgCl/KCl (sat'd)) displayed substantially lower cathode potentials, highlighting the beneficial role of CuO in enhancing HER activity. As shown in Fig. 4b, the enclosed area of the CV curves correlates with the electron storage capacity of the catalyst. Both MgO/CuO-SSM and CuO-SSM exhibit higher capacitance compared to SSM, indicating that CuO incorporation enhances charge storage.[47] In contrast, MgO-SSM exhibited limited redox activity, suggesting that MgO provides mainly structural benefits rather than electrocatalytic ones. Interestingly, after inoculation, MgO/CuO-SSM outperformed all other electrodes, exhibiting the highest electron storage capacity (Fig. 4c).

At −1 V *vs.* Ag/AgCl/KCl (sat'd), current for MgO/CuO-SSM (−4.22 mA) was 2.65-fold higher than that for CuO-SSM (−1.59 mA), 3.27 times higher than that for MgO-SSM (−1.29 mA) and nearly 12-fold higher than that for bare SSM (−0.36 mA). This significant increase in current confirms improved catalytic activity[48] and validates the effectiveness of the co-deposition strategy. Although MgO is an insulator with a wide band gap (>7.8 eV)[49] and does not inherently contribute to the electrode conductivity, previous studies have shown that MgO doping or MgO-based composites can achieve improved HER efficiencies during electrolysis.[50,51] Consistent with this, Nyquist plots (Fig. 4d and S3) revealed that MgO/CuO-SSM had the lowest impedance, followed by MgO-SSM, CuO-SSM, and finally bare SSM with the highest resistance. Notably, MgO deposition on CuO-SSM reduced the ohmic resistance (R_1) from 4.43 ± 0.09 Ω to 3.38 ± 0.02 Ω, compared to 3.91 ± 0.03 Ω for MgO-SSM and 8.17 ± 0.32 Ω for SSM. This reduction likely arises from lower contact resistance between the electrode and the current collector. Moreover, the inset of Fig. 4d shows that MgO-SSM (1.05 ± 0.04 Ω) had lower charge transfer resistance (R_2) than both CuO-SSM (4.46 ± 0.67 Ω) and SSM (5.11 ± 0.87 Ω). The

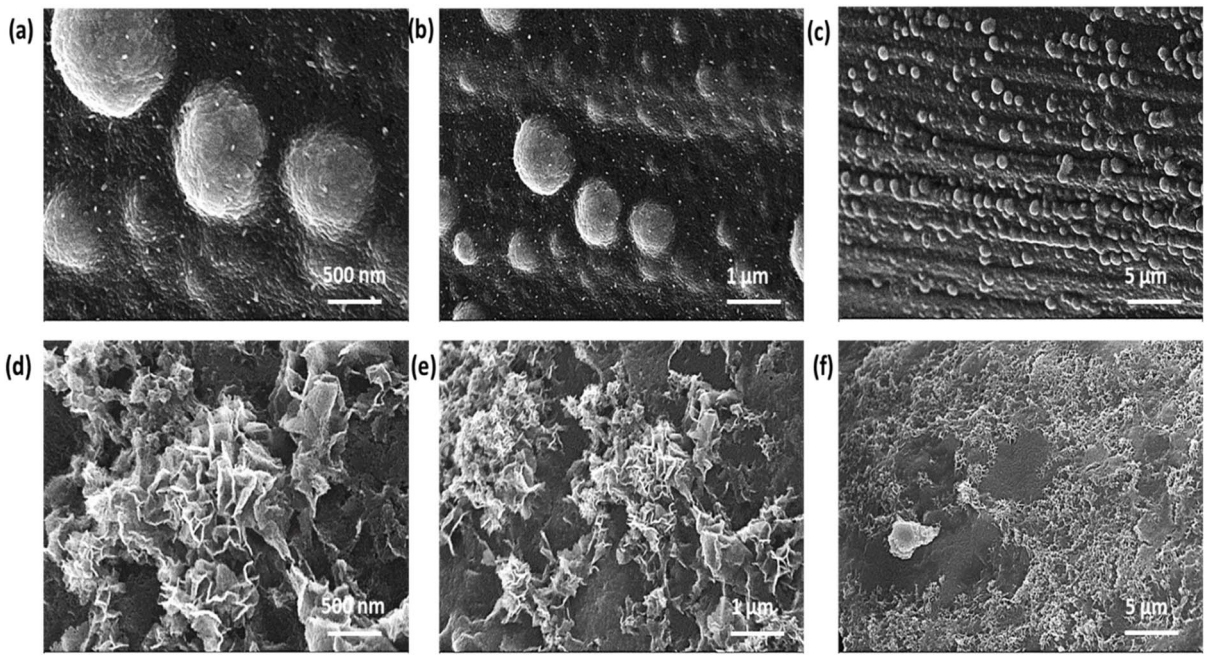

Fig. 3 SEM images at different magnifications. (a–c) CuO-SSM and (d–f) MgO/CuO-SSM.

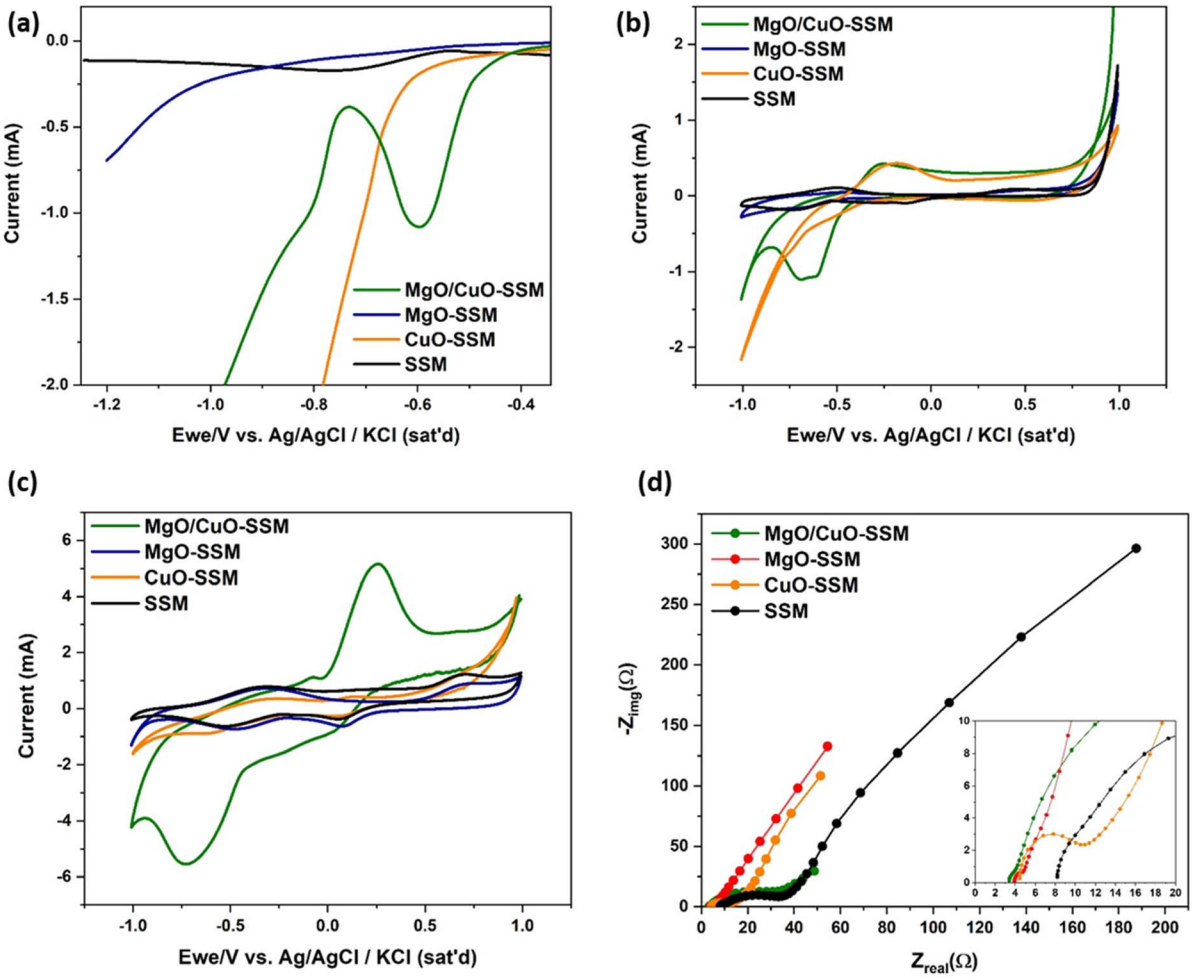

Fig. 4 LSV from −0.3 V to −0.9 V *vs.* Ag/AgCl/KCl (sat'd) (a), CV curve (b) at a scan rate of 5 mV s^{-1} under abiotic conditions, CV curves (c) and EIS (d) scanning from 100 kHz to 0.1 Hz at 10 mV amplitude during biotic experiments (at the end of operation). These analyses were conducted in a 3-electrode cell setting.

charge transfer resistance of the MgO/CuO-SSM composite was the lowest at 1.03 ± 0.04 Ω, suggesting that it could outperform CuO-SSM in CO_2 reduction performance.

3.2 Current density and hydrogen production

Inspired by the concept of the MES and guided by the performance of modified cathode catalysts, we established a hybrid bioelectrochemical system combining composite MgO/CuO-SSM, CuO-SSM, and bare SSM with CO_2-reducing microbial communities for biomethane production in electromethanogenesis systems such as the MES. The incorporation of CuO on SSM enabled higher current densities at an applied cathode potential of −1 V *vs.* Ag/AgCl/KCl (sat'd). After an enrichment period of 2 months, the MES cell with CuO-SSM recorded a current density of 3.05 A m^{-2}, followed by MgO/CuO-SSM (at 2.27 A m^{-2}) and bare SSM recording the lowest current density (1.99 A m^{-2}) in cycle 1 (Fig. 5a and b). After 4 cycles, CuO-SSM achieved the highest average current density, reaching 7.58 A m^{-2} compared to 3.96 and 3.22 A m^{-2} for MgO/CuO-SSM and bare SSM, respectively, attributed to its enhanced conductivity and electron transfer capacity.[52] Although the current densities increased substantially for modified cathodes (cycles 1–4 after enrichment at −1 V *vs.* Ag/AgCl/KCl (sat'd)), it was not significantly better than SSM (*t*-test, $p > 0.05$).

During the first operational stage (cycles 1–4, −1 V *vs.* Ag/AgCl/KCl (sat'd) applied cathode potential), H_2 was detected along with acetate (Fig. 5c and S4). For bare SSM, operating at relatively low current densities (<3.22 A m^{-2}), all H_2 gas produced was consumed for CH_4 production, with no residual H_2 detected in headspace gas. In contrast, MgO/CuO-SSM and CuO-SSM electrodes produced significant amounts of unused H_2, with a maximum of 291.6 ± 3.9 L(H_2) m^{-3}(catholyte replaced) d^{-1} and 625 ± 9.4 L(H_2) m^{-3}(catholyte replaced) d^{-1}, respectively, in cycle 2. This accumulation of H_2 at higher current densities could be associated with the following: (i) at a more negative cathode potential, increased current often lowers H_2 uptake efficiency and deteriorates MES stability[53,54] and (ii) higher HER potential on SSM compared to MgO/CuO-SSM and CuO-SSM (as observed in CV analysis) likely slows

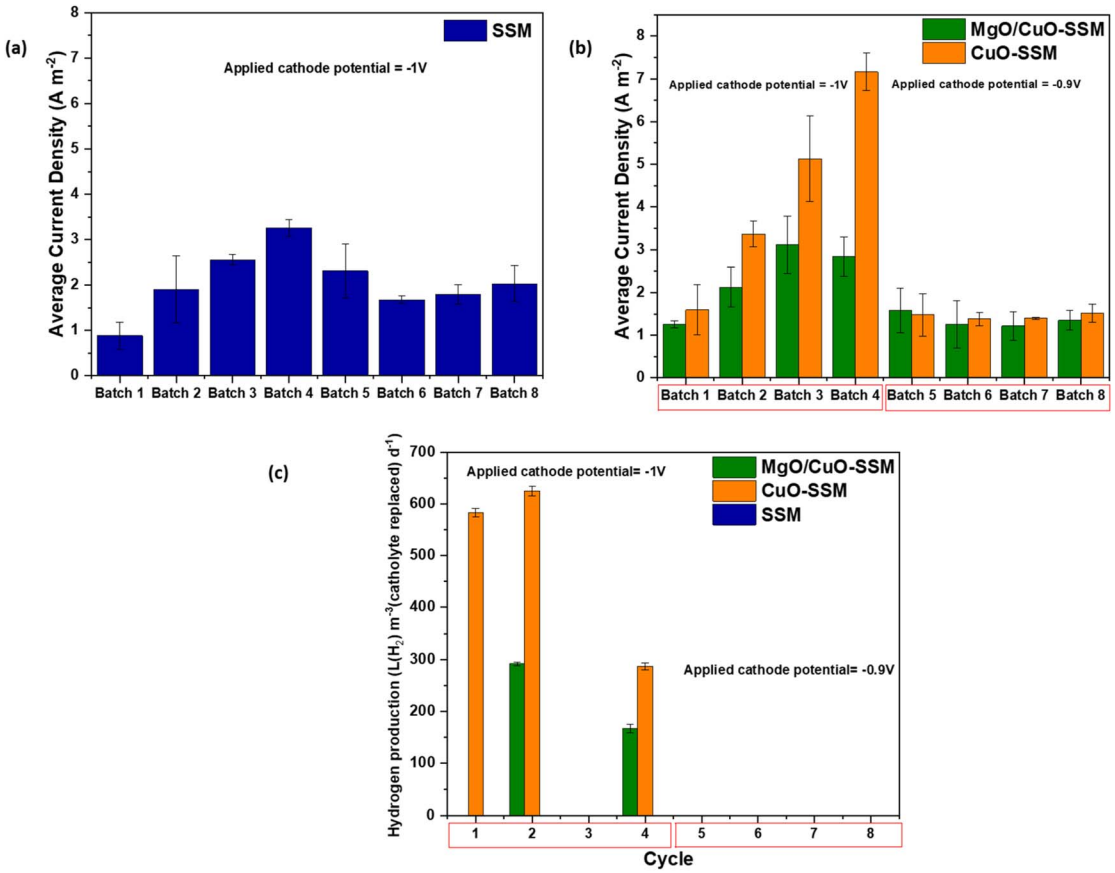

Fig. 5 The average current densities for MES reactors with SSM (a), MgO/CuO-SSM, and CuO-SSM (b), and H_2 produced (c) from semi-batch cycles. *Note*: SSM was operated at −1 V vs. Ag/AgCl/KCl (sat'd) throughout the experiment.

the HER while favouring direct methanogenesis, explaining the absence of H_2 in its headspace gas. Conversely, metal oxide-modified catalysts with lower charge-transfer resistance favour HER kinetics, leading to higher H_2 evolution. To address this, during the second stage of operation (cycles 5–8), the applied cathode potential was reduced to −0.9 V *vs.* Ag/AgCl/KCl (sat'd) for the modified electrodes, while bare SSM remained at −1 V *vs.* Ag/AgCl/KCl (sat'd). As expected, lowering the applied cathode potential reduced the current density and eliminated H_2 accumulation for MgO/CuO-SSM and CuO-SSM, while increasing the CH_4 content in the headspace biogas. The average current density of the MES using SSM was 1.8 ± 0.28 A m^{-2} at a cathode potential of -1 V *vs.* Ag/AgCl/KCl (sat'd), which was significantly higher (*t*-test, $p < 0.05$) than that of MgO/CuO-SSM and CuO-SSM at 1.3 ± 0.09 A m^{-2} and 1.4 ± 0.16 A m^{-2}, respectively, at a cathode potential of −0.9 V *vs.* Ag/AgCl/KCl (sat'd) (cycles 5–8).

3.3 Biogas production and energy efficiency

The MES reactors were initiated at −1 V *vs.* Ag/AgCl/KCl (sat'd) (up to cycle 4), and the data presented were recorded after an acclimation period of over 60 days. As discussed earlier, increased current densities with the modified electrodes resulted in enhanced gas production rates, predominantly consisting of H_2 and CO_2, with no or little CH_4 detected for MgO/CuO-SSM. This could be attributed to the different cathode catalyst employed in the MES reactors, exhibiting superior HER kinetics compared to bare SSM. CH_4 production rates were low at −1 V *vs.* Ag/AgCl/KCl (sat'd), which could result from CO_2 reduction to acetic acid rather than to CH_4.[55] As seen in Fig. 6a–c, CH_4 content eventually increased for modified electrodes as the applied cathode potential was reduced to −0.9 V *vs.* Ag/AgCl/KCl (sat'd), creating more suitable conditions for the biocathodes. This eventually improved the CH_4 productivity in MgO/CuO-SSM-based MES reactors. In terms of total gas volume produced at −1 V *vs.* Ag/AgCl/KCl (sat'd) (Fig. S5a–c), CuO-SSM generated the highest total gas output (625 ± 9.4 L(biogas) m^{-3}(catholyte replaced) d^{-1}), followed by MgO/CuO-SSM (291.6 ± 3.9 L(biogas) m^{-3}(catholyte replaced) d^{-1}) and SSM (203.7 ± 314.2 L(biogas) m^{-3}(catholyte replaced) d^{-1}), primarily H_2 for modified electrodes and a mixture of CO_2 and CH_4 for SSM. This indicates nearly 100% H_2 uptake efficiency for SSM, while MgO/CuO-SSM and SSM exhibited lower H_2 utilization. Thus, to enhance H_2 consumption and CO_2 reduction to CH_4, the applied cathode potential for MgO/CuO-SSM and CuO-SSM catalysts was reduced to −0.9 V *vs.* Ag/AgCl/KCl (sat'd) (Fig. 6d). At a lowered current density produced, high amounts of unused H_2 produced in biogas were nearly used for CH_4 or acetate production. The MES using MgO/

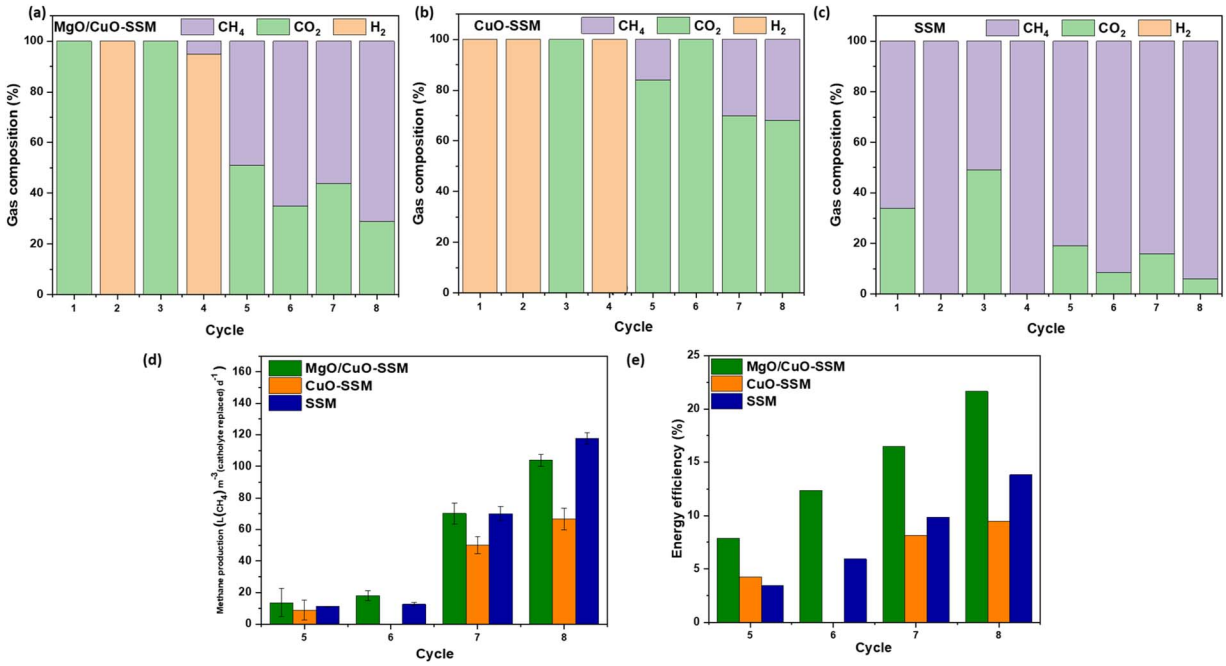

Fig. 6 Biogas composition (%) (a–c), methane production rate (d), and (e) electrical energy efficiencies from MES reactors. Note: SSM was operated at −1 V vs. Ag/AgCl/KCl (sat'd) throughout the experiment, while modified electrodes were at −0.9 V vs. Ag/AgCl/KCl (sat'd) from cycle 5 onwards.

CuO-SSM produced 13.6 ± 8.8 L(CH_4) m^{-3}(catholyte replaced) d^{-1} of CH_4 during the initial preliminary cycles at reduced cathode potential, with a maximum rate of 103.8 ± 3.8 L(CH_4) m^{-3}(catholyte replaced) d^{-1} for cycle 8. CuO-SSM had an 8-fold increase in CH_4 production, with the maximum reaching 66.67 ± 6.8 L(CH_4) m^{-3}(catholyte replaced) d^{-1} (Cycle 8). While SSM was operated at −1 V *vs.* Ag/AgCl/KCl (sat'd), it recorded 117.5 ± 3.6 L(CH_4) m^{-3}(catholyte replaced) d^{-1} of CH_4, suggesting a higher energy requirement by SSM for a comparable performance.

Furthermore, electrical energy conversion efficiency was calculated for all MES reactors based on methane production, confirming that the total energy consumption was much higher than the energy output for each reactor, resulting in a net negative energy balance (Fig. S5d). This is typical of MESs, as anodic water electrolysis requires high energy to overcome the thermodynamic barrier.[35] Considering that modified electrodes operated at less negative cathode potential (−0.9 V *vs.* Ag/AgCl/KCl (sat'd)), lowering the external cathode potential supply decreased the electrical energy input by 18.2% for CuO-SSM and 43.9% for MgO/CuO-SSM, compared to SSM (6.6 kJ) maintained at −1 V *vs.* Ag/AgCl/KCl (sat'd). While the energy input for MgO/CuO-SSM was the lowest (3.7 kJ), it produced a comparable CH_4 production rate of 103.8 ± 3.8 L(CH_4) m^{-3}(catholyte replaced) d^{-1} *vs.* 117.5 ± 3.6 L(CH_4) m^{-3}(catholyte replaced) d^{-1} for SSM (6.6 kJ) at the end of cycle 8. Ultimately, the net energy loss was reduced by 14% for CuO-SSM and 49.1% for MgO/CuO-SSM relative to SSM (5.7 kJ). Accordingly, the electrical energy efficiency for MgO/CuO-SSM was the highest at 21.6%, followed by SSM at 14.7%, and CuO-SSM at 9.5% at the end of the experiment (Fig. 6e). MES performance using MgO/CuO-SSM was higher than that of MES reactors with bare SSM cathodes (*t*-test, $p < 0.05$); however, statistical results were not significant for CuO-SSM (*t*-test, $p > 0.05$). It is crucial to understand that higher CH_4 production, as observed in this case, does not always correspond to higher energy efficiency. Instead, at a more negative applied potential, an increase in gaseous output could lead to higher energy input and lower overall electrical efficiency of the reactor. The superior performance of MgO/CuO-SSM could be attributed to the synergistic effect of MgO and CuO deposited on SSM, which reduces charge transfer resistance and thus lowers energy consumption for CH_4 production. Additionally, the mature MgO/CuO-SSM biocathode showed that higher current densities can increase H_2 availability, without compromising CH_4 generation at optimized cathode potentials. CuO-SSM exhibited superior HER activity but could not enhance CH_4 production and thus energy efficiency over bare SSM. Thus, cathode electrode modification could provide an energy-saving alternative potential for MES operation for biomethane production. However, maintaining a balance between the applied cathode potential/cell voltage and the methanogenesis capacity of the biofilms is essential for achieving energy-efficient MES operation.

3.4 Microbial community analysis

The impact of modified cathode catalysts on the microbial community composition was investigated using 16S rRNA sequencing. To better understand this, microbial communities were analyzed at both phylum and genus levels (Fig. 7). Among the archaeal communities (Fig. 7a) at the cathodes in the MES,

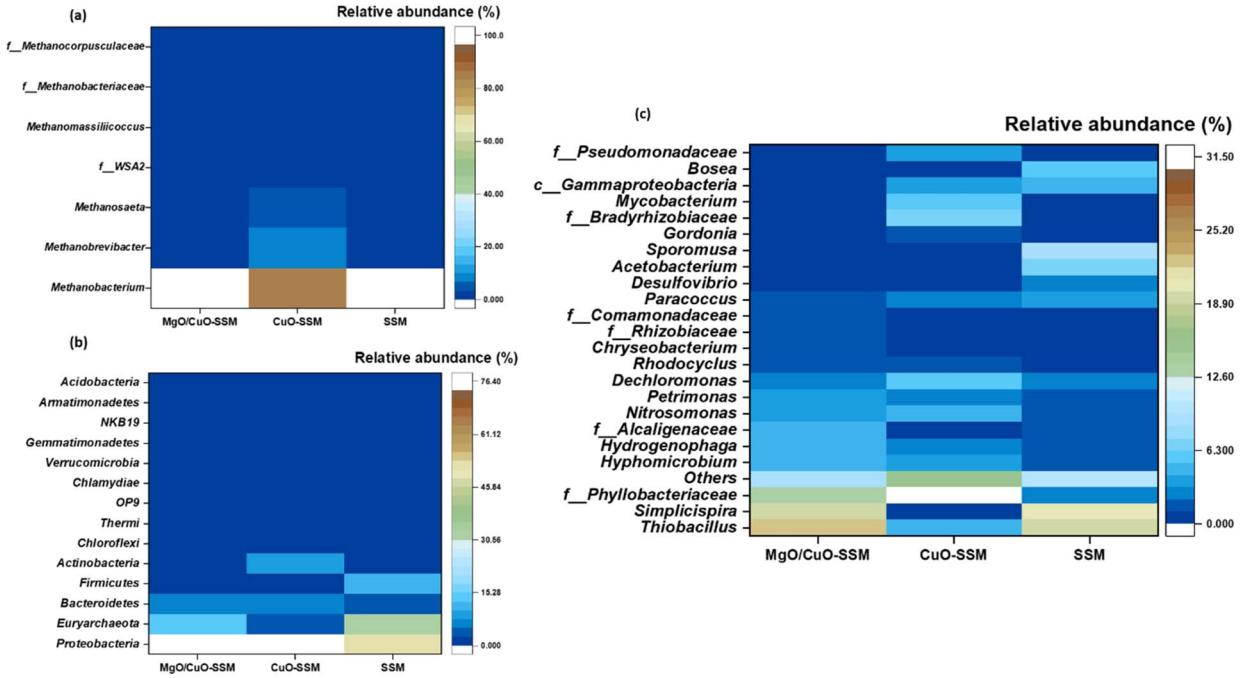

Fig. 7 Heatmap showing microbial communities in the cathode biofilms of the MES; (a) archaeal communities; (b) bacterial communities at the phylum level; (c) bacterial communities at the genus level.

most of the microbial species were predominantly *Methanobacterium*, *Methanobrevibacter*, and *Methanosaeta*. *Methanobacterium* play a crucial role in methane production in the MES by regulating the hydrogenotrophic methanogenesis pathway ($4H_2 + CO_2 \rightarrow CH_4 + 2H_2O$) and are also capable of using electro-methanogenesis ($CO_2 + 8H^+ + 8e^- \rightarrow CH_4 + 2H_2O$) at biocathodes.[35] *Methanobacterium* exhibited a relative abundance of 100% on SSM, followed by 99% *Methanobacterium* and 1% *Methanobrevibacter* on MgO/CuO-SSM. CuO-SSM exhibited 87% *Methanobacterium*, 7% *Methanobrevibacter*, and 4% *Methanosaeta*. Other archaeal members of the family *WSA2*, *Methanobacteriaceae*, and *Methanocorpusculaceae* were also present but at low (<1%) abundance. During the operation with bicarbonate as the CO_2 source, the cathodic biofilms confirmed the enrichment of *Proteobacteria* (51–76%), *Euryarchaeota* (3–31%), *Bacteroidetes* (4–7%), and *Firmicutes* (2–11%) at the phylum level (Fig. 7b). *Firmicutes* and *Bacteroidetes* found were associated with acetate synthesis, accounting for 15% of the communities at SSM, followed by 9% for CuO-SSM and 8% for MgO/CuO-SSM. This aligns with the acetate concentration in the MES reactors.[56]

At the genus level, dominant communities include *Thiobacillus* (4–23%), *Simplicispira* (1–20%), and members of the family *Phyllobacteriaceae* (3–31%) (Fig. 7c). Other minor genera include *Hyphomicrobium*, *Hydrogenophaga*, *Nitrosomonas*, and *Comamonadaceae* and the genera *Rhodocyclus*, *Acetobacterium*, *Sporomusa*, and *Desulfovibrio*, ranging between 1 and 4%. *Thiobacillus* and *Simplicispira* were most abundant in MgO/CuO-SSM (23%), moderate on SSM (19%), and lowest on CuO-SSM (4%). *Thiobacillus*, *Comamonadaceae* and its genus *Hydrogenophaga* exhibited higher abundance in the MES using MgO/CuO-SSM over SSM, suggesting autotrophic H_2 oxidation, commonly seen in MES biocathodes.[48] *Rhodocyclus* is known to contribute to H_2 production, collectively supporting enhanced H_2 production. *Acetobacterium* and *Sporomusa* were more abundant on SSM (7–9%), consistent with electron utilization for CO_2 reduction to acetate rather than CH_4. *Desulfovibrio* was detected at similar levels (1–2%) across all electrodes engaging in syntrophic interactions with methanogens.[57]

Interestingly, despite being an active abiotic electrocatalyst, CuO-SSM demonstrated poor microbial response. This is likely due to its antibacterial properties, particularly against anaerobic archaea like *Methanobacterium*, which impairs extracellular electron transfer and suppresses direct CO_2 reduction to CH_4.[58,59] Additionally, surface passivation and redox cycling of CuO between Cu^{2+}, Cu^+, and Cu^0 can increase toxicity and hinder biofilm stability. In contrast, MgO, though an electrical insulator, exhibited counterintuitive benefits when deposited on SSM or CuO. The rough and porous MgO layer served as a biocompatible scaffold for microbial adhesion and extracellular electron transfer.[60] Moreover, MgO stabilized CuO activity while enabling electron transport to the underlying CuO, where the HER occurred. This synergistic effect enhanced H_2/CO_2 adsorption, improved HER performance, and provided a more favourable niche for methanogenic and sulfur-reducing communities.[61]

Together, these findings highlight the role of catalyst–microbe interaction in determining MES performance. The catalyst-modified SSM in the MES, compared to SSM, could increase the active surface area to maximize CO_2 reduction. Additionally, the deposition of hydrophilic nanostructures could enhance the surface area-to-volume ratio necessary to

resolve the cathode packing density issue for large-scale applicability. However, to further improve the advantages associated with this approach, future studies should focus on systematically optimizing the ratio of dual active sites introduced, such as MgO and CuO in this study, to achieve a balance between the biocompatibility and electrocatalytic activity. While CuO is conductive and offers low charge-transfer resistance, its poor microbial compatibility limits methanogen enrichment, particularly *Methanobacterium*, which plays a pivotal role in hydrogenotrophic methanogenesis. Conversely, deposition of alkali metal oxide enhanced the surface biocompatibility, facilitating the growth of methanogenic communities, but caused moderate improvement in methane yield. Thus, tailoring the MgO/CuO ratio or the inclusion of other biocompatible oxides could be used to develop electrodes that couple HER kinetics and electro-methanogenesis with stable bacterial colonization. Other alternatives, such as doping, surface structuring, and scalable fabrication techniques, should be explored to address the trade-off between the productivity and efficiency of MESs. Our work represents a significant step, demonstrating that a simple, low-cost MgO/CuO nanocomposite can transform SSM into a highly functional cathode electrode in MESs. Although optimization of the catalyst remains necessary, the role of electrode-microbe interaction in achieving high energy efficiency has been highlighted. Mitigation of Cu toxicity by Mg without compromising catalytic activity provides a rational design principle that could be adopted for future electrodes, addressing the inhibition caused by high product concentrations.

4. Conclusions

This study investigated the modification of SSM by coupling MgO and a CuO-SSM cathode for CO_2 conversion to biomethane in an MES. The MgO overlayer improved the hydrophilicity, biocompatibility, and electron transfer, stabilizing CuO and mitigating its poor biocompatibility. At −0.9 V *vs.* Ag/AgCl/KCl (sat'd), MgO/CuO-SSM achieved CH_4 production rate of 103.8 ± 3.8 L(CH_4) m^{-3}(catholyte replaced) d^{-1} with the highest electrical energy efficiency of 21.6%, while SSM achieved the highest CH_4 yield (117.5 ± 3.6 L(CH_4) m^{-3}(catholyte replaced) d^{-1}) but at a lower energy efficiency (13.8%). This underscores the trade-off between productivity and energy efficiency in the MES. Combining MgO with CuO favoured the enrichment of hydrogenotrophic methanogens over the CuO-based electrode. Overall, this simple yet effective modification strategy transforms low-cost SSM into a highly functional cathode, addressing key limitations in energy efficiency, selectivity, and kinetics in the MES. These findings advance the potential of the MES as a scalable, sustainable technology for renewable energy generation and biogas refinement.

Author contributions

Simran Kaur Dhillon: conceptualization, data curation, formal analysis, investigation, methodology, visualization, writing-original draft; Tae Hyun Chung: formal analysis, investigation, methodology, writing – review & editing; Bipro Ranjan Dhar: conceptualization, funding acquisition, investigation, methodology, project administration, resources, supervision, writing – review & editing.

Conflicts of interest

The authors declare that they have no known competing financial interests or personal relationships that could have appeared to influence the work reported in this paper.

Data availability

Data will be made available on request.

Supplementary information (SI): Fig. S1: Schematic representation of a dual-chamber MES reactor configuration with an abiotic anode and a biotic cathode electrode, separated by Nafion TM 117 (PEM); Fig. S2: XRD patterns of all cathodes (a) and SEM images at different magnifications, (b and c) SSM and (d and e) MgO-SSM; Fig. S3: Equivalent circuit used (a) and resistances (b) from EIS fitting; Fig. S4: Acetate production at the end of each cycle; and Fig. S5: Biogas production rates from the MES equipped with MgO/CuO-SSM (a), CuO-SSM (b) at −0.9 V *vs.* Ag/AgCl/KCl (sat'd), SSM (c) cathodes at −1 V *vs.* Ag/AgCl/KCl (sat'd), and electrical energy balance for MES reactors based on methane output (d) for cycle 8. See DOI: https://doi.org/10.1039/d5se01460c.

Acknowledgements

This work was supported by the Natural Sciences and Engineering Research Council of Canada (NSERC) Discovery Grant, the Canada Research Chair (Tier 2) in Microbial Electrocatalysis for Energy and Environment, and the Canadian Foundation for Innovation (CFI) John R. Evans Leaders Fund (JELF).

References

1 O. Awogbemi and D. A. Desai, Novel technologies for CO_2 conversion to renewable fuels, chemicals, and value-added products, *Discover Nano*, 2025, **20**(1), 29.
2 K. P. Nevin, T. L. Woodard, A. E. Franks, Z. M. Summers and D. R. Lovley, Microbial electrosynthesis: feeding microbes electricity to convert carbon dioxide and water to multicarbon extracellular organic compounds, *mBio*, 2010, **1**(2), 10–128.
3 F. Tanguay-Rioux, E. Nwanebu, M. Thadani and B. Tartakovsky, On-line current control for continuous conversion of CO_2 to CH_4 in a microbial electrosynthesis cell, *Biochem. Eng. J.*, 2023, **197**, 108965.
4 A. B. Nelabhotla and C. Dinamarca, Bioelectrochemical CO_2 reduction to methane: MES integration in biogas production processes, *Appl. Sci.*, 2019, **9**(6), 1056.
5 G. Baek, K. Y. Kim and B. E. Logan, Impact of surface area and current generation of microbial electrolysis cell electrodes inserted into anaerobic digesters, *Chem. Eng. J.*, 2021, **426**, 131281.

6 J. S. Deutzmann, M. Sahin and A. M. Spormann, Extracellular enzymes facilitate electron uptake in biocorrosion and bioelectrosynthesis, *mBio*, 2015, **6**(2), 10–128.
7 T. H. Chung, S. K. Dhillon, C. Shin, D. Pant and B. R. Dhar, Microbial electrosynthesis technology for CO_2 mitigation, biomethane production, and ex-situ biogas upgrading, *Biotechnol. Adv.*, 2024, **77**, 108474.
8 G. Baek and B. E. Logan, A comprehensive analysis of key factors influencing methane production from CO_2 using microbial methanogenesis cells, *Water Res.*, 2023, **245**, 120657.
9 N. J. Claassens, C. A. Cotton, D. Kopljar and A. Bar-Even, Making quantitative sense of electromicrobial production, *Nat. Catal.*, 2019, **2**(5), 437–447.
10 R. M. Rodrigues, X. Guan, J. A. Iñiguez, D. A. Estabrook, J. O. Chapman, S. Huang, E. M. Sletten and C. Liu, Perfluorocarbon nanoemulsion promotes the delivery of reducing equivalents for electricity-driven microbial CO_2 reduction, *Nat. Catal.*, 2019, **2**(5), 407–414.
11 Y. Zhang, X. Y. Zhang and W. Y. Sun, In situ carbon-encapsulated copper-doped cerium oxide derived from MOFs for boosting CO_2-to-CH_4 electro-conversion, *ACS Catal.*, 2023, **13**(2), 1545–1553.
12 G. Baek, R. Rossi, P. E. Saikaly and B. E. Logan, High-rate microbial electrosynthesis using a zero-gap flow cell and vapor-fed anode design, *Water Res.*, 2022, **219**, 118597.
13 F. Geppert, D. Liu, E. Weidner and A. ter Heijne, Redox-flow battery design for a methane-producing bioelectrochemical system, *Int. J. Hydrogen Energy*, 2019, **44**(39), 21464–21469.
14 Z. Mao, S. Cheng, Y. Sun, Z. Lin, L. Li and Z. Yu, Enhancing stability and resilience of electromethanogenesis system by acclimating biocathode with intermittent step-up voltage, *Bioresour. Technol.*, 2021, **337**, 125376.
15 N. Yu, B. Bian, P. E. Saikaly, H. Zhang, K. Guo and B. E. Logan, High-rate and energy-efficient microbial electrosynthesis of methane using 3D dual-layer cathodes, *Chem. Eng. J.*, 2025, 165006.
16 Z. Zhang, Y. Song, S. Zheng, G. Zhen, X. Lu, T. Kobayashi, K. Xu and P. Bakonyi, Electro-conversion of carbon dioxide (CO_2) to low-carbon methane by bioelectromethanogenesis process in microbial electrolysis cells: The current status and future perspective, *Bioresour. Technol.*, 2019, **279**, 339–349.
17 A. Gomez Vidales, S. Omanovic and B. Tartakovsky, In-situ electrodeposition of nickel on a biocathode to enhance methane production from carbon dioxide in a microbial electrosynthesis system, *ECS Trans.*, 2020, **97**(7), 565–572.
18 S. Georgiou, L. Koutsokeras, M. Constantinou, R. Majzer, J. Markiewicz, M. Siedlecki, I. Vyrides and G. Constantinides, Microbial electrosynthesis inoculated with anaerobic granular sludge and carbon cloth electrodes functionalized with copper nanoparticles for conversion of CO2 to CH4, *Nanomaterials*, 2022, **12**(14), 2472.
19 S. Bajracharya, A. ter Heijne, X. D. Benetton, K. Vanbroekhoven, C. J. Buisman, D. P. Strik and D. Pant, Carbon dioxide reduction by mixed and pure cultures in microbial electrosynthesis using an assembly of graphite felt and stainless steel as a cathode, *Bioresour. Technol.*, 2015, **195**, 14–24.
20 D. Marcelo and A. Dell'Era, Economical electrolyser solution, *Int. J. Hydrogen Energy*, 2008, **33**(12), 3041–3044.
21 J. M. Olivares-Ramírez, M. L. Campos-Cornelio, J. U. Godínez, E. Borja-Arco and R. H. Castellanos, Studies on the hydrogen evolution reaction on different stainless steels, *Int. J. Hydrogen Energy*, 2007, **32**(15), 3170–3173.
22 K. P. Kuhl, T. Hatsukade, E. R. Cave, D. N. Abram, J. Kibsgaard and T. F. Jaramillo, Electrocatalytic conversion of carbon dioxide to methane and methanol on transition metal surfaces, *J. Am. Chem. Soc.*, 2014, **136**(40), 14107–14113.
23 K. P. Kuhl, E. R. Cave, D. N. Abram and T. F. Jaramillo, New insights into the electrochemical reduction of carbon dioxide on metallic copper surfaces, *Energy Environ. Sci.*, 2012, **5**(5), 7050–7059.
24 S. Nitopi, E. Bertheussen, S. B. Scott, X. Liu, A. K. Engstfeld, S. Horch, B. Seger, I. E. Stephens, K. Chan, C. Hahn and J. K. Nørskov, Progress and perspectives of electrochemical CO_2 reduction on copper in aqueous electrolyte, *Chem. Rev.*, 2019, **119**(12), 7610–7672.
25 M. Jiang, Y. Gao, S. A. Patil, H. Hou, W. Feng and S. Chen, Reactive coating modification of metal material with strong bonding strength and enhanced corrosion resistance for high-performance bioelectrode of microbial electrochemical technologies, *J. Power Sources*, 2021, **491**, 229595.
26 G. Baek, R. Rossi, P. E. Saikaly and B. E. Logan, The impact of different types of high surface area brush fibers with different electrical conductivity and biocompatibility on the rates of methane generation in anaerobic digestion, *Sci. Total Environ.*, 2021, **787**, 147683.
27 G. Baek, L. Shi, R. Rossi and B. E. Logan, Using copper-based biocathodes to improve carbon dioxide conversion efficiency into methane in microbial methanogenesis cells, *Chem. Eng. J.*, 2022, **435**, 135076.
28 O. Y. Bisen and K. K. Nanda, Alkaline earth metal based single atom catalyst for the highly durable oxygen reduction reaction, *Appl. Mater. Today*, 2020, **21**, 100846.
29 K. Karthikeyan, S. Amaresh, V. Aravindan and Y. S. Lee, Microwave assisted green synthesis of MgO–carbon nanotube composites as electrode material for high power and energy density supercapacitors, *J. Mater. Chem. A*, 2013, **1**(12), 4105–4111.
30 D. Bejjanki, S. K. Puttapati, H. Pant and V. V. Srikanth, Novel MgO/few-layer graphene-filled polyaniline ternary nanocomposite as efficient electrode material in aqueous supercapacitors, *Bull. Mater. Sci.*, 2023, **46**(1), 48.
31 A. Mondal, M. Sultana and A. Paul, Understanding the Mechanism of CO_2 to CH_4 Conversion and Hydrogen Evolution Reaction on Mg Nanoparticles in Water under ambient conditions: A DFT Perspective, *Int. J. Hydrogen Energy*, 2025, **168**, 150978.
32 J. Zhang, H. Jiang, J. Gao, L. Zhang, C. Zhao and H. Suo, In situ fabrication of copper oxide nanoparticles decorated

carbon cloth for efficient electrocatalytic detection of nitrite, *Microchem. J.*, 2023, **194**, 109302.
33 M. T. Mhetre, S. M. Mane, J. Lee and B. J. Lokhande, Electrodeposited three-dimensional hierarchical architecture of MgO anchored with Ag nanoparticles for high-performance symmetric supercapacitors, *J. Energy Storage*, 2024, **89**, 111774.
34 S. K. Dhillon, A. Chaturvedi, D. Gupta, T. C. Nagaiah and P. P. Kundu, Copper nanoparticles embedded in polyaniline derived nitrogen-doped carbon as electrocatalyst for bio-energy generation in microbial fuel cells, *Environ. Sci. Pollut. Res.*, 2022, **29**(53), 80787–80804.
35 T. H. Chung, S. K. Dhillon, A. A. Chakrabarty and B. R. Dhar, Simultaneous Biogas Upgrading and Desulfurization Using a Microbial Electrosynthesis System with Optimized Electrodes and Membrane Selection, *ACS ES&T Eng.*, 2025, **5**(9), 2224–2237.
36 E. Bolyen, J. R. Rideout, M. R. Dillon, N. A. Bokulich, C. C. Abnet, G. A. Al-Ghalith, H. Alexander, E. J. Alm, M. Arumugam, F. Asnicar and Y. Bai, Reproducible, interactive, scalable and extensible microbiome data science using QIIME 2, *Nat. Biotechnol.*, 2019, **37**(8), 852–857.
37 R. C. Edgar, Search and clustering orders of magnitude faster than BLAST, *Bioinformatics*, 2010, **26**(19), 2460–2461.
38 K. Kardarian, D. Nunes, P. M. Sberna, A. Ginsburg, D. A. Keller, J. V. Pinto, J. Deuermeier, A. Y. Anderson, A. Zaban, R. Martins and E. Fortunato, Effect of Mg doping on Cu_2O thin films and their behavior on the TiO_2/Cu_2O heterojunction solar cells, *Sol. Energy Mater. Sol. Cells*, 2016, **147**, 27–36.
39 M. Zhang, X. Ma, S. Wang, Z. Cao and H. Zhong, Dual modification of stainless steel by small molecule oxalic acid for oxygen evolution reaction, *ACS Sustain. Chem. Eng.*, 2023, **11**(17), 6765–6773.
40 N. Alahmadi, H. S. Alhasan, H. Gomaa, A. A. Abdelwahab and M. Y. Emran, Electrochemical sensor design based on CuO nanosheets/Cellulose derivative nanocomposite for hydrazine monitoring in environmental samples, *Microchem. J.*, 2022, **183**, 107909.
41 S. H. Tu, H. C. Wu, C. J. Wu, S. L. Cheng, Y. J. Sheng and H. K. Tsao, Growing hydrophobicity on a smooth copper oxide thin film at room temperature and reversible wettability transition, *Appl. Surf. Sci.*, 2014, **316**, 88–92.
42 A. Bougharouat, N. Touka, D. Talbi and K. Baddari, Hydrophobic properties of CuO thin films obtained by sol-gel spin coating technique-annealing temperature effect, *Ann. Chim. Phys.*, 2021, **45**, 439–445.
43 A. Kondo, R. Kurosawa, J. Ryu, M. Matsuoka and M. Takeuchi, Investigation on the mechanisms of $Mg(OH)_2$ dehydration and MgO hydration by near-infrared spectroscopy, *J. Phys. Chem. C*, 2021, **125**(20), 10937–10947.
44 N. M. Adhikari, A. Tuladhar, Z. Wang, J. J. De Yoreo and K. M. Rosso, No hydrogen bonding between water and hydrophilic single crystal MgO surfaces, *J. Phys. Chem. C*, 2021, **125**, 26132–26138.
45 M. Li, M. N. Idros, Y. Wu, T. Burdyny, S. Garg, X. S. Zhao, G. Wang and T. E. Rufford, The role of electrode wettability in electrochemical reduction of carbon dioxide, *J. Mater. Chem. A*, 2021, **9**(35), 19369–19409.
46 Z. Zeng, X. Wu, Y. Liu, C. Chen, D. Tian, Y. He, L. Wang, G. Yang, X. Zhang and Y. Zhang, Fabrication of a durable coral-like superhydrophilic MgO coating on stainless steel mesh for efficient oil/water separation, *Chem. Eng. Sci.*, 2022, **248**, 117144.
47 B. Bian, N. Yu, A. Akbari, L. Shi, X. Zhou, C. Xie, P. E. Saikaly and B. E. Logan, Using a non-precious metal catalyst for long-term enhancement of methane production in a zero-gap microbial electrosynthesis cell, *Water Res.*, 2024, **259**, 121815.
48 Y. He, J. Li, L. Zhang, X. Zhu, Y. Pang, Q. Fu and Q. Liao, 3D-printed GA/PPy aerogel biocathode enables efficient methane production in microbial electrosynthesis, *Chem. Eng. J.*, 2023, **459**, 141523.
49 D. M. Roessler and W. C. Walker, Electronic spectrum and ultraviolet optical properties of crystalline MgO, *Phys. Rev.*, 1967, **159**(3), 733.
50 H. Tan, B. Tang, Y. Lu, Q. Ji, L. Lv, H. Duan, N. Li, Y. Wang, S. Feng, Z. Li and C. Wang, Engineering a local acid-like environment in alkaline medium for efficient hydrogen evolution reaction, *Nat. Commun.*, 2022, **13**(1), 2024.
51 R. Li, X. Zhu, X. Yan, H. Kobayashi, S. Yoshida, W. Chen, L. Du, K. Qian, B. Wu, S. Zou and L. Lu, Oxygen-controlled hydrogen evolution reaction: molecular oxygen promotes hydrogen production from formaldehyde solution using Ag/MgO nanocatalyst, *ACS Catal.*, 2017, **7**(2), 1478–1484.
52 I. Vassilev, H. Yao, S. Shakeel, M. Tuominen, A. Heponiemi, D. Bergna, U. Lassi and M. Kokko, Impregnation of granular activated carbon with nickel or copper improves performance of microbial electrosynthesis, *Bioresour. Technol.*, 2025, **418**, 131914.
53 G. Shang, K. Cui, W. Cai, X. Hu, P. Jin and K. Guo, A 20 L electrochemical continuous stirred-tank reactor for high rate microbial electrosynthesis of methane from CO_2, *Chem. Eng. J.*, 2023, **451**, 138898.
54 J. N. Hengsbach, B. Sabel-Becker, R. Ulber and D. Holtmann, Microbial electrosynthesis of methane and acetate—comparison of pure and mixed cultures, *Appl. Microbiol. Biotechnol.*, 2022, **106**(12), 4427–4443.
55 J. Mueller, Microbial Catalysis of methane from carbon dioxide. The Future of Renewable Energy is Inside You, Doctoral dissertation, The Ohio State University, 2012.
56 I. Vassilev, P. Dessì, S. Puig and M. Kokko, Cathodic biofilms–A prerequisite for microbial electrosynthesis, *Bioresour. Technol.*, 2022, **348**, 126788.
57 C. Flores-Rodriguez and B. Min, Enrichment of specific microbial communities by optimum applied voltages for enhanced methane production by microbial electrosynthesis in anaerobic digestion, *Bioresour. Technol.*, 2020, **300**, 122624.
58 N. Aryal, L. Wan, M. H. Overgaard, A. C. Stoot, Y. Chen, P. L. Tremblay and T. Zhang, Increased carbon dioxide reduction to acetate in a microbial electrosynthesis reactor with a reduced graphene oxide-coated copper foam composite cathode, *Bioelectrochemistry*, 2019, **128**, 83–93.

59 K. R. Chatzipanagiotou, V. Soekhoe, L. Jourdin, C. J. Buisman, J. H. Bitter and D. P. Strik, Catalytic cooperation between a copper oxide electrocatalyst and a microbial community for microbial electrosynthesis, *ChemPlusChem*, 2021, **86**(5), 763–777.

60 M. Li, S. Zhou and M. Xu, Graphene oxide supported magnesium oxide as an efficient cathode catalyst for power generation and wastewater treatment in single chamber microbial fuel cells, *Chem. Eng. J.*, 2017, **328**, 106–116.

61 X. Zheng, Y. Zhou, X. Liu, X. Fu, H. Peng and S. Lv, Enhanced adsorption capacity of MgO/N-doped active carbon derived from sugarcane bagasse, *Bioresour. Technol.*, 2020, **297**, 122413.

62 A. A. Ragab, D. R. Shaw, K. P. Katuri and sP. E. Saikaly, Effects of set cathode potentials on microbial electrosynthesis system performance and biocathode methanogen function at a metatranscriptional level, *Sci. Rep.*, 2020, **10**(1), 19824.

63 S. Fu, I. Angelidaki and Y. Zhang, In situ biogas upgrading by CO2-to-CH4 bioconversion, *Trends Biotechnol.*, 2021, **39**(4), 336–347.

